



Heterostructured CNT-RuSx nanomaterials for efficient electrochemical hydrogen evolution reaction

Changgen Cheng^{a,1}, Weidong Ao^{a,1}, Huijun Ren^{a,1}, Zhengyuan Shen^{a,1}, Zhishuai Fan^a, Tingting Xu^b, Wei Liu^{c,*}, Qi Zhang^{d,*}, Peiqun Yin^{b,*}, Lei Dai^{a,*}

^a Key Laboratory for Special Functional Materials of Ministry of Education, School of Materials Science and Engineering, Henan University, Kaifeng 475004, China

^b Center of Biomedical Materials Research and Engineering, School of Biomedical Engineering, Anhui Medical University, Hefei 230032, China

^c State Key Laboratory of Fine Chemicals, School of Chemical Engineering, Dalian University of Technology, Dalian 116024, China

^d Institute of Industry & Equipment Technology, Hefei University of Technology, Hefei 230009, China

ARTICLE INFO

Keywords:

CNT-RuSx

In-situ construction strategy

Amorphous

Abundant C-S-Ru interfaces

Electrochemical hydrogen evolution

ABSTRACT

Heterostructured CNT-RuSx nanomaterials have been prepared by a facile and straightforward in-situ construction strategy. The obtained CNT-RuSx with abundant C-S-Ru interfaces demonstrates excellent catalytic hydrogen evolution activity comparable to commercial Pt/C. To afford a current density of 10 mA/cm², the required overpotential was only 17 mV with a smaller Tafel slope of 35 mV/dec in 1 M KOH. Meanwhile, the outstanding catalytic stability is also achieved on CNT-RuSx, no obviously degradation in performance during long-term electrolysis under basic conditions. Theoretical calculations show that the C-S-Ru interfaces will facilitate the dissociation of water and reduce the free energy of H adsorption, thereby leading to dramatically enhanced hydrogen evolution performance. This work provides a technical guidance for the rational design and synthesis of novel C-based commercial catalysts for renewable energy conversion systems.

1. Introduction

Commercial noble metal catalysts are widely used in electrochemical energy conversion systems, such as water splitting to produce hydrogen [1–5]. As the most excellent hydrogen evolution catalyst, commercial Pt/C exhibits exceptional hydrogen evolution activity, providing an optimal benchmark for evaluating electrocatalysts performance [6,7]. However, Pt suffers from limited reserves and prohibitive cost. In addition, a multitude of studies have confirmed that commercial Pt/C cannot maintain stable hydrogen evolution activity as a cathode catalyst [8–12]. Commercial Pt/C consists of conductive carbon spheres and Pt nanoparticles, and Pt nanoparticles are only physically adsorbed on the surface of the carbon spheres. During the electrolysis process, Pt nanoparticles will reunite together and result in a decrease in catalytic activity. Therefore, opening a novel synthetic strategy to access electrocatalysts with high activity and stability to replace commercial Pt/C is essential for the development of green hydrogen production.

The latest researches indicates that Ru-based nanomaterials can efficiently catalyze the hydrogen evolution process in acidity and

alkalinity, and their activity is satisfactory as alternatives of Pt [13–21]. More importantly, Ru has abundant reserves and low price, which is more conducive to large-scale production. However, the carriers are still necessary to endow Ru-based catalysts with high stability and excellent hydrogen evolution activity, which attributed to the formation of a unique interface between the Ru-based species and the carriers [12,15]. Carbon-based materials are the ideal carriers, such as carbon nanotubes (CNT) [22–26]. CNT has good electrical conductivity and can quickly export electrons in the electrocatalytic process. At the same time, the self-supporting one-dimensional structure can effectively prevent the occurrence of agglomeration during the catalytic process [25,27–29]. However, it is difficult to deposit metals or metal sulfides on the surface of CNT, due to physico-chemical properties of C. Therefore, developing a unique and rational synthesis strategy, to engineer Ru-based nanoparticles in-situ on the surface of CNT, and form C-Ru heterostructures, as the efficient heterostructured electrocatalyst for hydrogen evolution, will be a breakthrough in material and renewable energy science.

In this work, we successfully achieve the direct synthesis of ruthenium sulfide (RuSx) nanoparticles tightly anchored on the surface of

* Corresponding authors.

E-mail addresses: liuweikd@dlut.edu.cn (W. Liu), zhangq@hufut.edu.cn (Q. Zhang), pqyin@mail.ustc.edu.cn (P. Yin), dailei@henu.edu.cn (L. Dai).

¹ These authors contributed equally to this work.

CNT by an in-situ construction strategy. The construction process consists of two aspects: Initially, the CNT were heat treated with ammonium sulfide to form CNT-S. Subsequently, the CNT-S were mixed with Ru precursor and heated, and RuSx nanoparticles were finally formed ascribed to the chelation of S and Ru. Concurrently, RuSx nanoparticles will tightly anchor on the surface of CNT in-situ to form CNT-RuSx. Due to the existence of abundant C-S-Ru interface, the obtained CNT-RuSx possesses remarkable catalytic hydrogen evolution activity, exceeding the commercial Pt/C. In 1 M KOH, to output a current density of 10 mA/cm², the required overpotential on the CNT-RuSx is only 17 mV with a smaller Tafel slope of 35 mV/dec, which is better than that of commercial Pt/C (45 mV, 68 mV/dec, respectively). Excellent catalytic stability is also achieved on CNT-RuSx, and the chronoamperometry curves show that the current density can still be maintained at 320 mA/cm² during 40 h of electrolysis when an overpotential of 200 mV is applied. Theoretical calculations show that the C-S-Ru interface will facilitate the dissociation of water and reduce the free energy of H adsorption, contributing to the excellent HER performance.

2. Materials and methods

Chemicals: Ruthenium chloride (RuCl₃), Lanthanum chloride (LaCl₃), Cerium chloride (CeCl₃), Sodium chloropalladate (Na₂PbCl₄), Potassium chloroplatinite (K₂PtCl₄), Ammonium sulfide solution ((NH₄)₂S, 20–26% in H₂O), Commercial Pt/C (10%), Potassium hydroxide (KOH, 85%), Dimethylformamide (DMF), acetone and ethanol were purchased from Aladdin. Multi-walled carbon nanotubes (CNT) were purchased from LG Chem. The Milli-Q water used in all experiments with a resistivity of 18.2 MΩ cm was prepared using a Milli-Q water system.

2.1. Characterizations

Transmission electron microscopic investigation was carried out using a high-resolution transmission electron microscope (JEOL, JEM-2100 F and JEM-2010) operated at 200 kV and TECNAI F-30 operated at 300 kV. Scanning electron microscopy (SEM) imaging was recorded by JSM-7900 F SEM. The elemental content is measured by inductively coupled plasma mass spectrometry (NeXION 2000 G). The surface area of the material is measured by nitrogen adsorption isotherms (Quantachrome Autosorb iQ3MVC). The XANES spectra of C K-edge, S K-edge and Ru M-edge were measured at the Catalysis and surface Science End station at the BL11U beamline of National Synchrotron Radiation Laboratory (NSRL) in Hefei. The Ru K-edge X-ray absorption fine structure data were gleaned at 14B2 station in Super Photon ring-8 GeV in Japan. The Ru K-edge XANES data were recorded in a transmission mode. The acquired EXAFS data were extracted and processed according to the standard procedures using the ATHENA module implemented in the IFEFFIT software packages. The phase purity of the as-prepared sample was characterized by X-ray diffraction (D8-ADVANCE) with Cu KR radiation from 10° to 80° at a scanning rate of 10°/min. XPS data were acquired using an AXIS SUPRA+ X-ray photoelectron spectroscope incorporating a 165 mm hemispherical electron energy analyzer. The Raman spectroscopy was carried out by Renishaw inVia, VERTEX 70 with a 532 nm laser. Contact angle measurements were performed on a DSA25 (KRÜSS) at room temperature.

2.2. Experiment section

2.2.1. Synthesis of sulfur-modified CNT (CNT-S)

To synthesize CNT-S, 10 mg of CNT and 1 mL of (NH₄)₂S were co-dissolved in 10 mL of DMF. Next, the mixture was then sealed in a 30-mL pressure vessel and heated from room temperature to 170 °C in 30 min, then held at 170 °C for 10 h. The light black product was collected by centrifugation (6000 rpm, 2 min) and rinsed 3 times with acetone to remove excess (NH₄)₂S.

2.2.2. Synthesis of CNT-RuSx

To synthesize CNT-RuSx, 10 mg of the obtained CNT-S and 0.1 mmol of RuCl₃ were co-dissolved in 2 mL of water and 8 mL of DMF. Next, the mixture was sealed in a 30-mL pressure glass vessel and heated from room temperature to 140 °C in 30 min and then held at 140 °C for 6 h. The light blue product was collected by centrifugation (6000 rpm, 3 min) and rinsed 3 times with Milli-Q water.

2.2.3. Synthesis of CNT-MS (M= Ce, Pd, La, Pt)

The synthesis procedure is the same as CNT-RuSx, except that 0.1 mmol of other metal precursors were used instead of RuCl₃.

2.2.4. Synthesis of RuSx

To synthesize RuSx, 0.1 mmol of RuCl₃ and 1 mL of (NH₄)₂S were co-dissolved in 10 mL of DMF to form a dark brown solution. Next, the solution was sealed in a 30-mL pressure vessel and heated from room temperature to 140 °C in 30 min, and then kept at 140 °C for 10 h. The product was collected by centrifugation (10,000 rpm, 3 min) and rinsed 3 times with acetone.

2.3. XAFS fitting analysis

To obtain quantitative structural parameters around Ru atoms in the as-obtained CNT-RuSx and RuSx samples, least-squares curve fitting analysis was performed using the ARTEMIS module of IFEFFIT package. The fits were done in the R-space within the R-range of 1.0–2.3 Å for k²-weighted EXAFS oscillation function $\chi(k)$ data from 2.6 to 15.0 Å⁻¹. Taking the deviations from the Gaussian shape of first prominent FT peak into account, a two-shell structure model including a Ru-S and Ru-O shell was used to fit the EXAFS data of these two samples. Effective scattering amplitudes and phase shifts of all scattering paths were calculated by the ab initio code FEFF8.4. The coordination numbers N, interatomic distances R, DebyeWaller factor σ^2 , and the edge-energy shift ΔE_0 were treated as adjustable parameters. Following the above fitting strategy, we obtained satisfactory curve-fitting results as shown in Fig. S16, and the yielded parameters were listed in Tables S1.

2.4. Electrochemical test

All electrochemical tests are performed on the Chi760E and CS150M workstations with three-electrode setups. 0.1 mg of the sample and 5 μL of nafion solution (5%, D520) were dropped on a 1.0 cm² glassy carbon as the working electrode, a 1.0 cm² graphite flake was used as the counter electrode, and the saturated calomel electrode (SCE) was used as the reference electrode. 85% of resistance compensation is applied to all test processes. In 1 M KOH, $E(\text{RHE}) = E(\text{SCE}) + 0.2412 + \text{pH} \times 0.0592 = E(\text{SCE}) + 1.045$. The Nyquist plots were measured at frequency between 100 kHz and 0.1 Hz with an applied voltage amplitude of 1 mV at the −0.1 V vs RHE. The TOF values of the HER were calculated by the following equation: $\text{TOF} = I / (2Fn)$, where I is the current at different potential (A), F is the faraday constant with a value of 96485 C/mol, n is the number of moles of the catalysts on the electrode.

2.5. Computational methods

The density functional theory (DFT) calculations were performed with the Vienna Ab initio Simulation Package (VASP 5.4) based on projector augmented wave (PAW) method. Perdew-Burke-Ernzerhof (PBE) functional within generalized gradient approximation is adopted to treat electronic exchange-correlation energy. For C, RuS and RuS/C, integration in Brillouin zone is performed to optimize geometric configuration using the k-point mesh of $3 \times 3 \times 1$, $3 \times 3 \times 3$ and $3 \times 3 \times 1$ on the basis of the Monkhorst-Pack scheme. The plane-wave cutoff energy is set to 400 eV. The convergence criteria for structural optimization are set as 0.1×10^{-4} eV and 0.03 eV/Å for energy and force, respectively. The higher energy criteria of 0.1×10^{-6} eV is used for

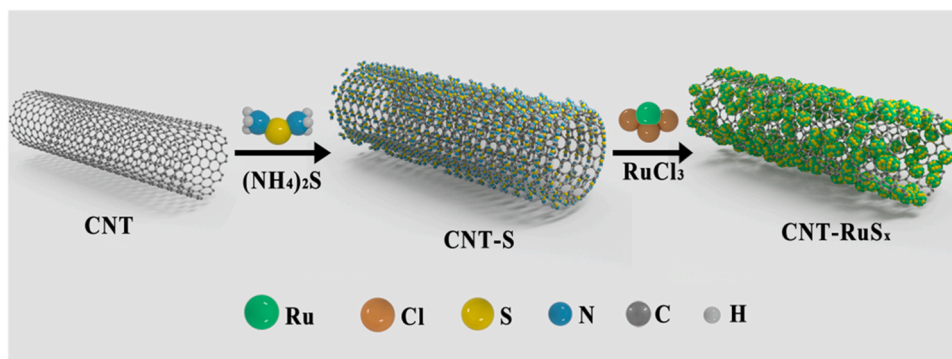


Fig. 1. The proposed formation mechanism of the heterostructured CNT-RuS_x.

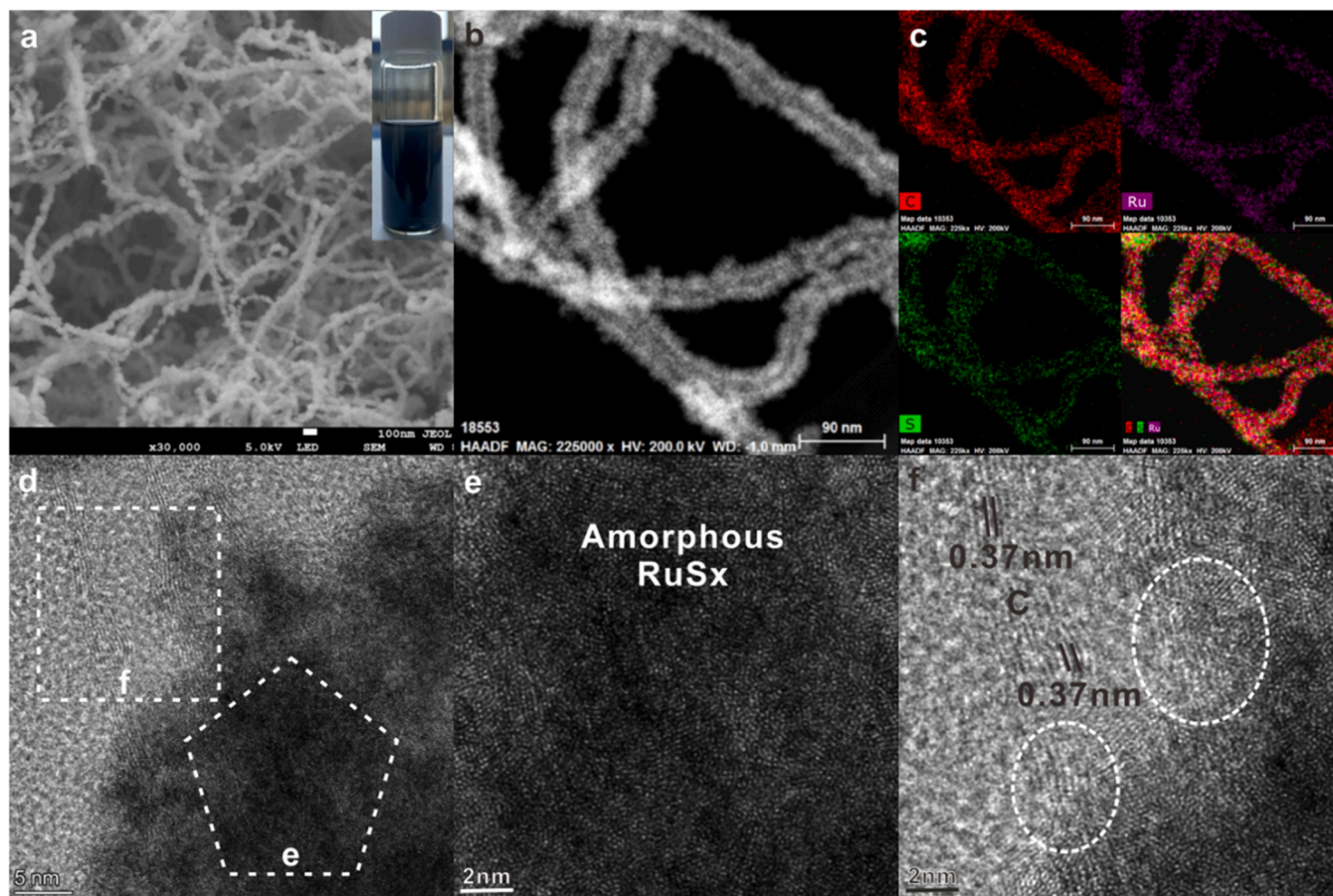


Fig. 2. Microscopic characterizations of the heterostructured CNT-RuS_x. (a) High-magnification SEM image. Inset: Photograph of a dispersion of the CNT-RuS_x in water. (b) HAADF-STEM image. (c) STEM-EDX elemental mappings. (d) HRTEM image of the CNT-RuS_x. The corresponding HRTEM images of (e) RuS_x and (f) CNT were marked in the dotted quadrilateral and pentagon, respectively, in (d). The oval in (f) showed the C-RuS_x interface.

vibrational frequency calculation. The vacuum layer of 20 Å is used to avoid interaction between adjacent layers. The climbing-image nudged elastic band (CI-NEB) method was employed to determine the kinetic barrier and transition state of water dissociation. The Gibbs free energy $\Delta G(H_2O)^*$ can be calculated as follows: $\Delta G(H_2O)^* = \Delta E(H_2O)^* + \Delta EZPE - T\Delta S(H_2O)^*$. $\Delta E(H_2O)^*$ is the adsorption energy of the H (H₂O) species. $\Delta EZPE$ is the difference in the zero-point energy of H (H₂O) in the adsorbed state and the gas phase. The entropy difference is denoted as $\Delta S(H_2O)^*$. T is the room temperature of 298 K.

3. Results and discussion

3.1. Electron microscopy and spectral characterization

The synthetic procedure of heterostructured CNT-RuS_x was experienced through a two-step route, as shown in Fig. 1, the CNT (Fig. S1) were first heat-treated with ammonia sulfide to form CNT-S (Fig. S2). After hydrothermal treatment, their morphology can be remained, which was confirmed by transmission electron microscope (TEM) and scanning electron microscopy (SEM). The signal of sulfur species appeared on the X-ray photoelectron spectroscopy (XPS) spectrum, indicating that S was successfully adsorbed on the surface of CNT

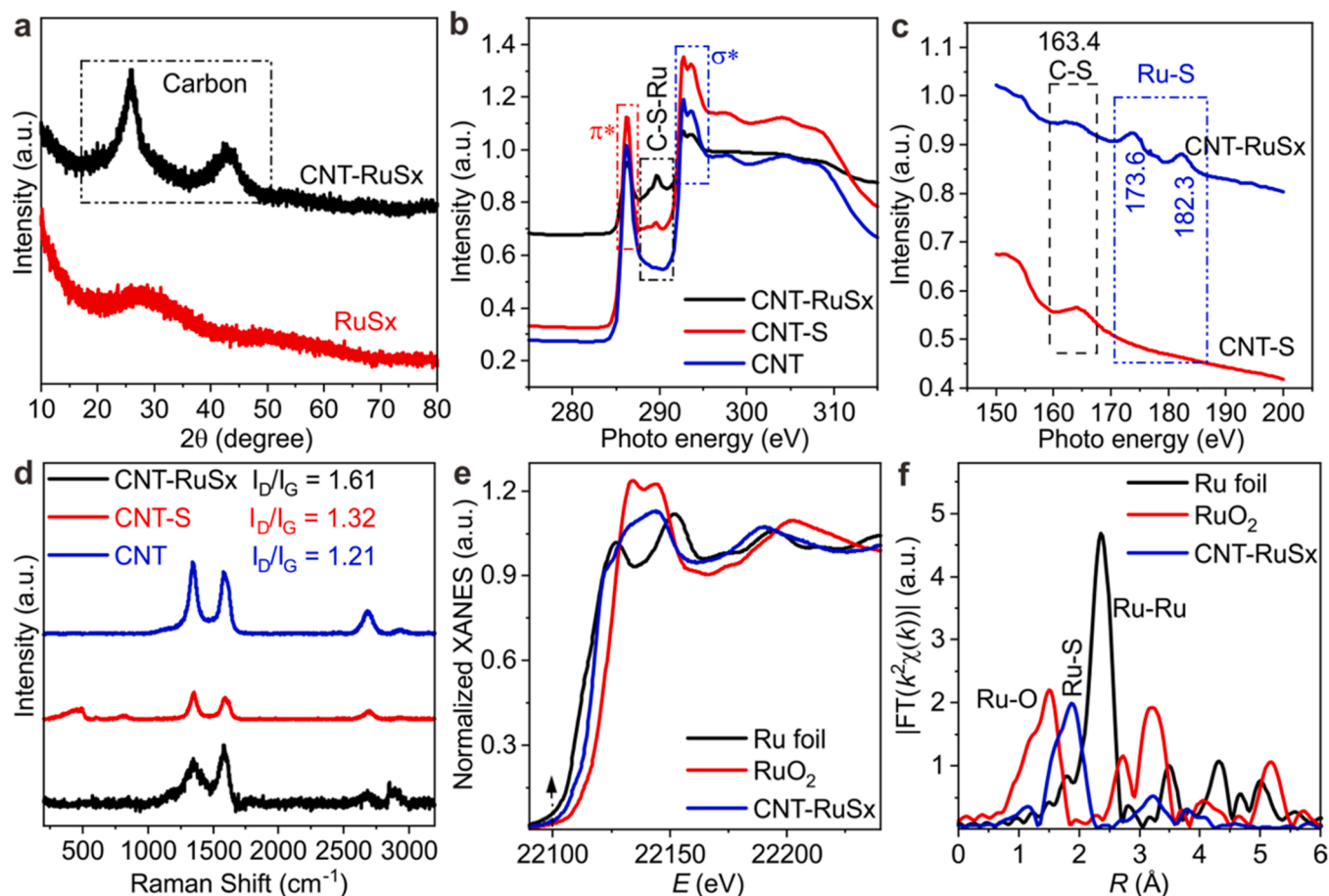


Fig. 3. Detailed structure characterizations of the heterostructured CNT-RuSx. (a) XRD pattern of the CNT-RuSx and RuSx. (b) C K-edge XANES spectra of CNT-RuSx, CNT-S and CNT. (c) S L-edge XANES spectra of CNT-RuSx and CNT-S. (d) Raman spectra of CNT, CNT-S and CNT-RuSx. (e) XANES and (f) the corresponding k^2 -weighted FT spectra in R-space at the Ru K-edge for CNT-RuSx. The data of Ru foil and RuO₂ are shown for references. In all images, the a.u. stands for arbitrary units.

(Fig. S3). Subsequently, the CNT-S were mixed with ruthenium chloride precursor and then heated. Finally, plenty RuSx nanoparticles was anchored in-situ on the surfaces of CNT to form high-density heterostructure attributed to the chelation between Ru and S existing on the surface of CNT. And the SEM images demonstrated that the CNT-RuSx is obtained in high quality and high yield and still maintains the original one-dimensional structure of CNT (Fig. 2a and S4). As proved by the dark-field scanning transmission electron microscopy (STEM) (Fig. 2b), RuSx nanoparticles are uniformly wrapped on the surface of the CNT to form an overall core-shell structure, which was further confirmed by energy dispersive X-ray (EDX) line-scanning analysis (Fig. S5). The elemental mappings of CNT-RuSx show the homogeneous distribution of C, S and Ru (Fig. 2c), and the atomic ratios of Ru:S:C (measured by Inductively Coupled Plasma-Mass) are estimated to be 2.4:2.7:95.9 (Fig. S6). As illustrated in high-resolution transmission electron microscopy (HRTEM) images, RuSx are in the amorphous phase, Ru atoms are randomly arranged in non-close-packed pattern. C is in the crystalline phase, and the crystal lattice with the lattice spacing of 3.7 Å, corresponding to the (200) plane of carbon (Fig. 2d-e). The low-crystalline of the CNT-RuSx was also confirmed by selected area electron diffraction (SEAD) pattern (Fig. S7) and the reduced peak intensity in the X-ray diffraction (XRD) pattern (Fig. 3A), only two broad diffraction peaks were appeared in XRD pattern, which belong to the characteristic peak of CNT (Fig. S8). No diffraction peaks of RuSx appear. Pure ruthenium sulfide (the atomic ratios of Ru:S measured by ICP-MS is estimated to be 1.0:1.4) is also in an amorphous state (Fig. 3a and S9). Such an amorphous structure has abundant defect sites and strong structural self-healing ability, which are conducive to the construction of efficient

and stable electrocatalysts [4,30–32]. It should be noted that RuSx cannot be uniformly loaded onto the surface of the CNT if we use the one-pot method (Figure 10a) or the two-step loading method (Figure 10b).

The chemical state of Ru and S in the CNT-RuSx was analyzed by XPS. As shown in Fig. S11, the binding energy peaks of Ru 3p are located at 462.2 and 484.4 eV, which can be assigned to Ru (III) [14,33]. Compared to pure RuSx nanoparticles (462.9 and 485.0 eV, respectively, Fig. S12), the binding energy peaks of CNT-RuSx slightly shift to lower binding energy, which can be attributed to the formation of C-S-Ru heterostructured interface. The binding energy peaks of S 2p located at 169.2 and 163.7 eV can be identified as signal of SO₃²⁻ (or SO₄²⁻) and S²⁻, respectively (Fig. S11 and S12). Moreover, the local electronic structures of the CNT-RuSx were further investigated by the X-ray absorption near edge structure (XANES) spectroscopy. As shown in C K-edge spectra (Fig. 3b), the peaks located at 288.5 and 294.3 eV can be assigned to the π^* orbital and σ^* band, respectively. Meanwhile, CNT-RuSx and CNT-S also exhibited a distinct peak at 290 eV, verifying the existence of C-S-Ru heterostructures in the samples [34–37]. The peak of S L-edge at 163.4 eV (Fig. 3c) further confirm the presence of C-S bond, coinciding with C K-edge spectra [24]. In addition, the peaks at 173.6 and 182.3 eV indicate the existence of the S-Ru bond. As illustrated in Fig. S13, the typical Ru M₂-edge and M₃-edge binding peaks of CNT-RuSx at 464.5 and 486.7 eV shift to lower energy, suggesting the electronic transfer from CNT or S to Ru, consistent with the formation of C-S-Ru interfaces. The formation of the C-S-Ru chemical interfaces will inevitably affect the Raman scattering of CNT. As shown in Fig. 3d, the typical D and G bands of carbon are located at 1357 and 1595 cm⁻¹,

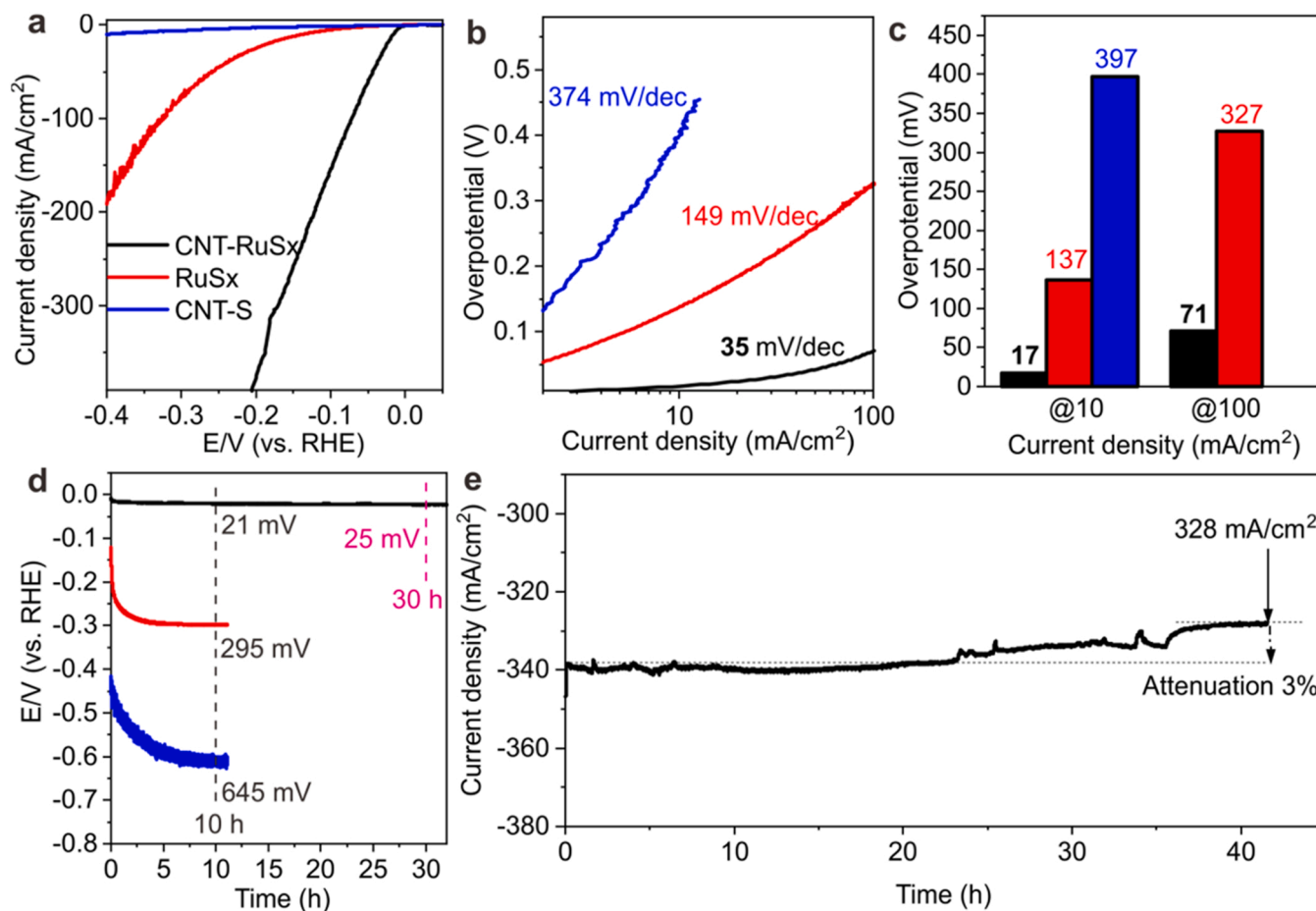


Fig. 4. HER performances of heterostructured CNT-RuSx (black line), RuSx (red line), and CNT-S (blue line) in 1.0 M KOH. (a) Electrode surface area-normalized polarization curves. The scan rate is 10 mV/s. (b) Corresponding Tafel plots obtained from (a). (c) The overpotentials required for an anodic current density of 10 and 100 mA/cm². (d) Chronopotentiometric curve of CNT-RuSx, RuSx, and CNT-S at 10 mA/cm². (e) Chronoamperometric curve of CNT-RuSx at -0.2 V (vs. RHE) for 40 h. The loading amounts of all catalysts on glassy carbon are 0.1 mg/cm².

respectively. The ratio of peak intensity of D and G (ID/IG) of CNT, CNT-S, and CNT-RuSx were 1.21, 1.32, and 1.61 respectively, which is corresponding to the defect density of carbon materials. The decrease of ID/IG value indicates that the defects on the CNT surface are gradually increased in these samples.

To further elucidate the fine atomic structure of CNT-RuSx, X-ray absorption fine structure (XAFS) spectroscopy measurements at the Ru K-edge were employed. As shown in the X-ray absorption near-edge spectra (XANES) in Fig. 3e, the absorption edge of CNT-RuSx evaluated from the half step height is located between that of Ru foil and RuO₂, manifesting an intermediate valance state of Ru between that of Ru(0) and Ru(IV). This observation is consistent with the XPS results. Notably, the pre-edge feature at ca. 22,110 eV resulting from formally electric dipole forbidden Ru 1 s → 4d transition, significantly intensified compared to that of RuO₂ reference. This suggests a local breaking of centrosymmetry in the sample [38]. Further extended X-ray absorption fine structure (EXAFS) data analysis was conducted to acquire the detailed structural information of Ru in CNT-RuSx (Fig. 3f). Notably, in the case of CNT-RuSx, the prominent peak at ca. 1.89 Å (without phase shift correction) was almost identical to that of RuSx, unambiguously demonstrating the Ru-S coordination (Fig. S14). We resort to quantitative EXAFS curve-fitting analysis to infer the Ru-S coordination number (*N*) of 4.7, and the indicated under-coordinated geometry is in consistent with the XANES analysis (Fig. S15 and Table S1). Close inspection shows that the main peak slightly deviates from a symmetrical Gaussian shape, pointing out the need to include Ru-O scattering path, which is presumably correlated with the pre-adsorbed oxygen (see discussions in

Table S1) [39]. Conclusively, all the aforementioned results corroborated the in-situ construction of ultrafine Ru-based sulfides on the surface of CNT with abundant C-S-Ru interfaces.

3.2. Electrochemical hydrogen evolution

The C-S-Ru heterostructures existed in electrocatalysts can play a critical role to improve the electrocatalytic activity and stability of the catalyst [40–44]. As a proof-of-concept application, the as-obtained CNT-RuSx was first employed for HER. Commercial Pt/C (Fig. S16), CNT-S and RuSx nanoparticles were used as control groups. As shown in Fig. 4a–4b and Table S2, CNT-RuSx exhibited competitive catalytic activity, to achieve a current density of 10 mA/cm² on the CNT-RuSx, the overpotential was 17 mV with a smaller Tafel slope of 35 mV/dec, which were much better than those of RuSx nanoparticles (137 mV, 149 mV/dec, respectively) and CNT-S (397 mV, 374 mV/dec, respectively), corroborating the strong ability of CNT-RuSx to dissociate water molecular. Strikingly, the catalytic hydrogen evolution performances of CNT-RuSx in alkaline conditions were better than that of commercial Pt/C (48 mV, 68 mV/dec, respectively, Fig. S17a). The smaller Tafel slope also allows CNT-RuSx to obtain large current densities at low potentials, for example, when obtaining a current density of 100 mA, the required overpotential was only 71 mV, which was much lower than 172 mV on commercial Pt/C (Fig. 4c and S17a). TOF values were calculated to illustrate the intrinsic activity of the catalysts. Fig. S18 shows that CNT-RuSx exhibits higher TOF values at the same potential regardless of the element-based accounting than RuSx. As revealed in

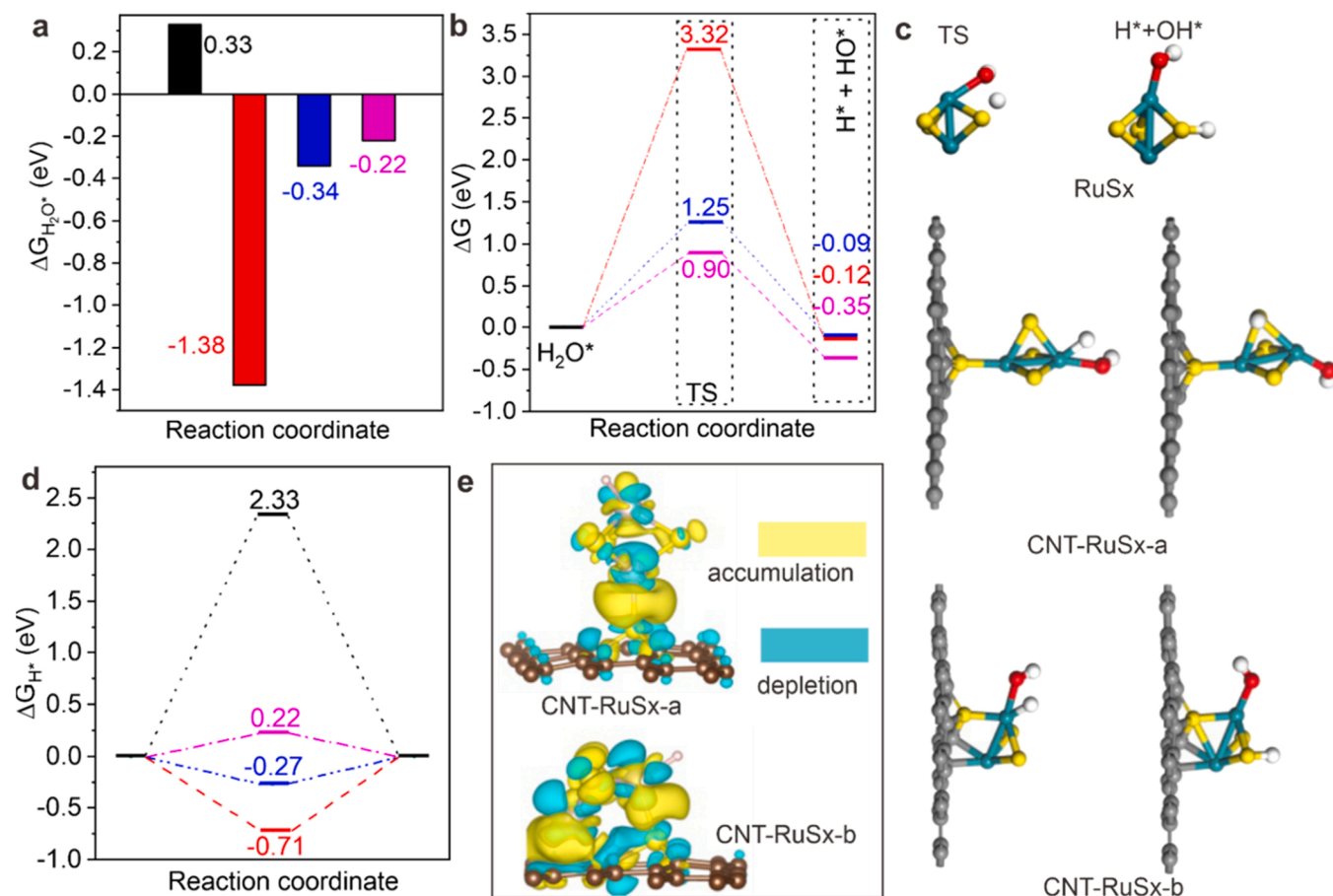


Fig. 5. Density functional theory calculations. (a) The calculated Gibbs water adsorption free energy ($\Delta G_{H_2O^*}$) on CNT-S (black line), RuSx (red line), CNT-RuSx-a (purple line), and CNT-RuSx-b (blue line). (b) Reaction energy diagram and (c) Adsorption model of water dissociation on RuSx, CNT-RuSx-a and CNT-RuSx-b. (d) The calculated Gibbs hydrogen adsorption free energy (ΔG_{H^*}) diagram on CNT-S (black line), RuSx (red line), CNT-RuSx-a (purple line), and CNT-RuSx-b (blue line). (e) Charge density difference of the CNT-RuSx-a and CNT-RuSx-b (Yellow and cyan regions represent electron accumulation and depletion, respectively).

Fig. 4d, CNT-RuSx possesses stability without negligible activity attenuation under a current density of 10 mA/cm², after 10 and 30 h of electrolysis, the required overpotentials on the CNT-RuSx are 21 and 25 mV, respectively. After careful measurement and calculation, the Faraday efficiency of hydrogen is ~98% during this stage (Fig. S19). On RuSx and CNT-S, after only 10 h of electrolysis, the required overpotential increases to 295 and 645 mV, respectively. It should be pointed out that the activity performance of Pt/C drops drastically after electrolysis within 2000 s due to lack of carrier support effect (S17b), highlighting the super catalytic stability of CNT-RuSx. It is worth noting that when overpotential of 200 mV is applied on CNT-RuSx, the acquired current density can be maintained at 320 mA/cm² during 40 h of electrolysis, which is close to the technical requirements of commercial electrochemical hydrogen production (Fig. 4e). These results undoubtedly manifest that CNT-RuSx has potential application value as a substitute for commercial Pt/C (Table S3).

3.3. DFT

In order to further understand the role of C-S-Ru heterostructures in water splitting and H-coupling, density functional theory (DFT) calculations were conducted to elucidate the superior HER performances of CNT-RuSx (Figs. S20). Combining the amorphous properties and XANES data of the samples, four models of CNT-S, RuSx, CNT-RuSx-a and CNT-RuSx-b were established [31,45,46]. For the alkaline HER, the H₂O molecule is first adsorbed, then dissociates to generate reactive H* intermediate followed by H* combination to form H₂. For the overall

process, the H₂O adsorption free energy ($\Delta G_{H_2O^*}$), H₂O dissociation energy barrier (ΔE^\ddagger) and H adsorption free energy (ΔG_{H^*}) are key descriptors to depict the HER activity [35,47]. The favorable water adsorption is prerequisite. The $\Delta G_{H_2O^*}$ of CNT-S is positive of 0.33 eV, indicating the unfavorable water adsorption. The CNT-RuSx-a and CNT-RuSx-b catalysts exhibit affable H₂O adsorption with $\Delta G_{H_2O^*}$ of -0.22 and -0.34 eV, respectively. As for RuSx, it binds too much tightly with $\Delta G_{H_2O^*}$ of -1.38 eV (Fig. 5a). For the following water dissociation, RuSx, CNT-RuSx-a and CNT-RuSx-b were investigated (Fig. 5b and c), and the dissociation processes are exergonic with energy changes of -0.12 eV, -0.35 and -0.09 eV, respectively. While the energy barriers on RuSx, CNT-RuSx-a and CNT-RuSx-b are 3.32, 1.25 and 0.90 eV, respectively. The pretty high energy barrier of 3.32 eV indicates rough H₂O dissociation to barely generate H* intermediate for RuSx catalyst. Despite the superior water adsorption, the difficult dissociation step makes RuSx not the preferred alkaline HER catalyst. By contrast, the CNT-RuSx catalysts (CNT-RuSx-a and CNT-RuSx-b), show more feasible H₂O dissociation. As to the generated H* intermediate, ΔG_{H^*} closes to zero meaning facile desorption and adsorption of H. As shown in Fig. 5d, the ΔG_{H^*} of S-doped carbon is as high as 2.33 eV, consistent with the rough H₂O adsorption. The H adsorption on RuSx catalyst becomes more feasible with much lower ΔG_{H^*} of -0.71 eV, reminding the highly tight H₂O adsorption. The CNT-RuSx-a and CNT-RuSx-b catalysts exhibit moderate strength hydrogen adsorption with ΔG_{H^*} of 0.22 eV and -0.27 eV, which are closer to 0 eV, meaning that CNT-RuSx has better hydrogen evolution activity. The charge density difference of CNT-RuSx-a and CNT-RuSx-b shows significant

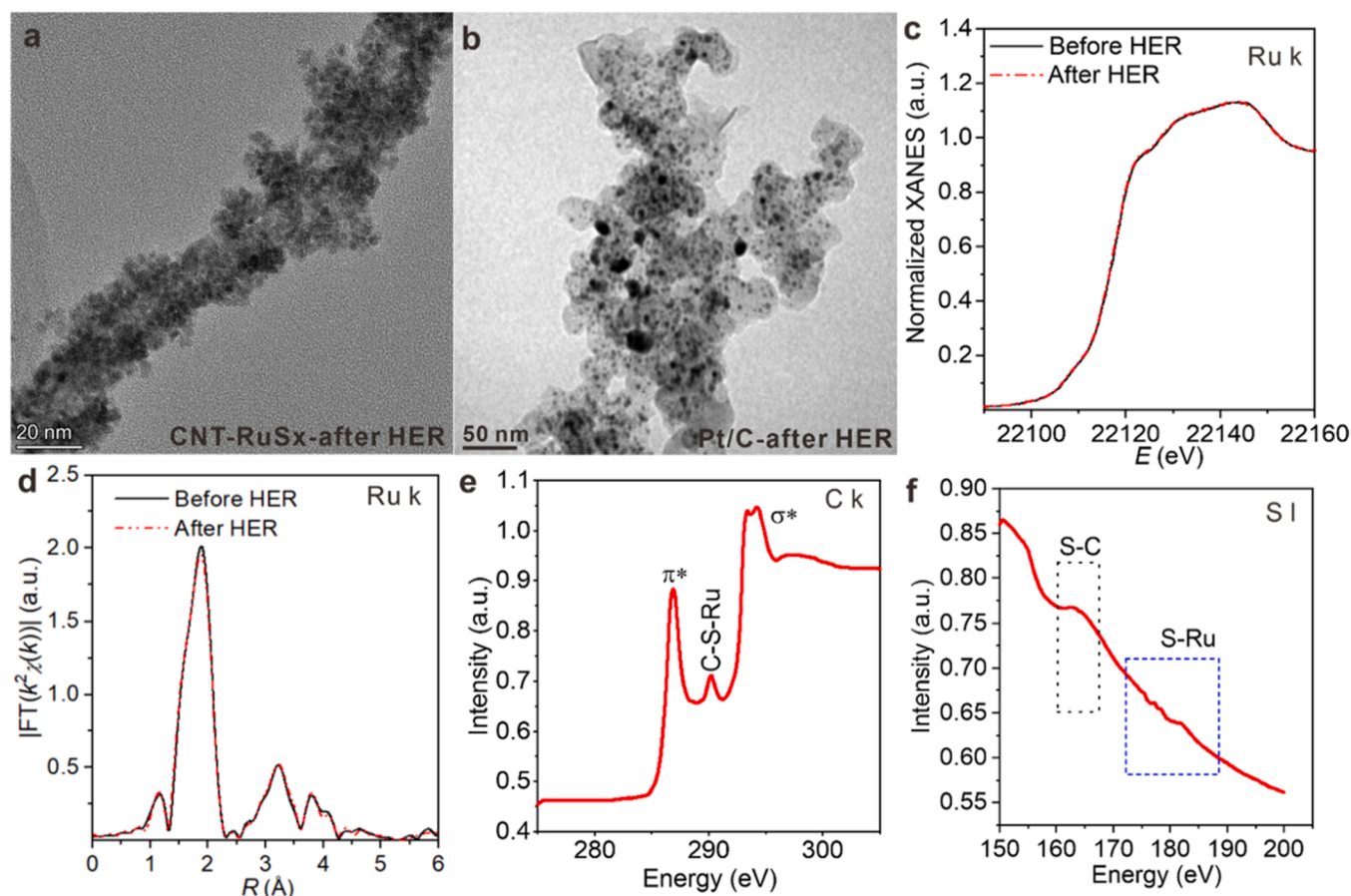


Fig. 6. Microscopic characterizations of the heterostructured CNT-RuSx after HER. (a) High-magnification TEM image of CNT-RuSx. (b) High-magnification TEM image of Pt/C. (c) XANES and (d) the corresponding k^2 -weighted FT spectra in R-space at the Ru K-edge for CNT-RuSx. (e) C K-edge and (f) S L-edge XANES spectra of CNT-RuSx. In all images, the a.u. stands for arbitrary units.

charge density accumulation between RuSx and carbon materials (Fig. 5e), which will weaken the strong interaction between H and RuSx. In summary, the CNT-RuSx delivers favorable H_2O adsorption, dissociation, feasible H adsorption and desorption, all contributing to the great HER activity.

3.4. Experimental exploration of active mechanism

Fig. S21 shows that CNT-RuSx and RuSx have relatively close physical specific surface areas, but the electrochemical hydrogen evolution performances of them are very different, so we reasonably speculate that the superior electrocatalytic HER performances of CNT-RuSx would be ascribed to the C-S-Ru heterostructures, which will bring favorable electron/mass transport ability, excellent hydrophilicity, and the large electrochemical active area. The charge transport kinetics in the electrocatalysis was investigated by electrical impedance spectroscopy (ESI) 1.0 M KOH. As illustrated in Fig. S22, the heterostructured CNT-RuSx displayed a smaller charge-transfer resistance of 1.0Ω than RuSx (42.8Ω) and CNT-S (173.4Ω), respectively, indicating the superior charge transport kinetics of C-S-Ru heterostructures during electrocatalysis. CNT-S possess theoretically ideal electron and substance transport capabilities, but its application is hampered by wettability [48]. As shown in Fig. S23, water cannot infiltrate the surface of CNT-S, triggering the poor transport ability of CNT-S. In contrast, water can infiltrate the surface of CNT-RuSx. Therefore, RuSx in C-S-Ru heterostructures acted as the active site to catalyze the decomposition of water and promote the coupling of H-H bonds. Meanwhile, the CNT can opportunely export electrons to prevent the occurrence of electronic lag and bring stable hydrogen evolution activity. Subsequently, to further

identify the intrinsic activity sites of the catalyst towards HER, the electrochemical double-layer capacitance (Cdl) could be probed to estimate the ECSA [49,50]. The cyclic voltammograms scanning of catalysts were recorded at the scan rate of 10–50 mV/s in 1.0 M KOH. As shown in Figs. S24–S25, the Cdl values of CNT-RuSx were 149.3 mF/cm^2 , which was much larger than that of RuSx (8.3 mF/cm^2), validating the higher specific surface area as well as substantial reaction active sites for HER. Importantly, after the stability test, the TEM image shows that the self-supporting 1D structure of heterostructured CNT-RuSx can be retained and RuSx nanoparticles are still wrapped on the surface of CNT (Fig. 6a). In contrast, the Pt nanoparticles in commercial Pt/C agglomerate severely to form larger-sized nanoparticles (Fig. 6b), resulted in the impressive decline of electrocatalytic performance. Moreover, XANES and the corresponding k^2 -weighted FT spectra in R-space at the Ru K-edge for CNT-RuSx have not changed significantly after electrocatalysis (Fig. 6c–6d). Meanwhile, CNT-RuSx also exhibited a distinct peak at 290 eV and peak of S L-edge at 163.4 eV (Fig. 3c), verifying the existence of C-S-Ru heterostructures in the samples after electrocatalysis. All the aforementioned results demonstrate that CNT-RuSx can be feasible to replace commercial Pt/C as the next generation highly efficient HER electrocatalyst.

3.5. Exploration of the universality of preparation methods

Besides, the general applicability of an unique synthesis method is extremely important for materials science. In this work, the in-situ construction strategy was also effective in the synthesis of other CNT-MSx (M = Ce, Pd, La, Pt, etc.) heterostructured materials. Fig. 7 shows typical STEM images of the as-prepared CNT-CeSx, CNT-PdSx, CNT-

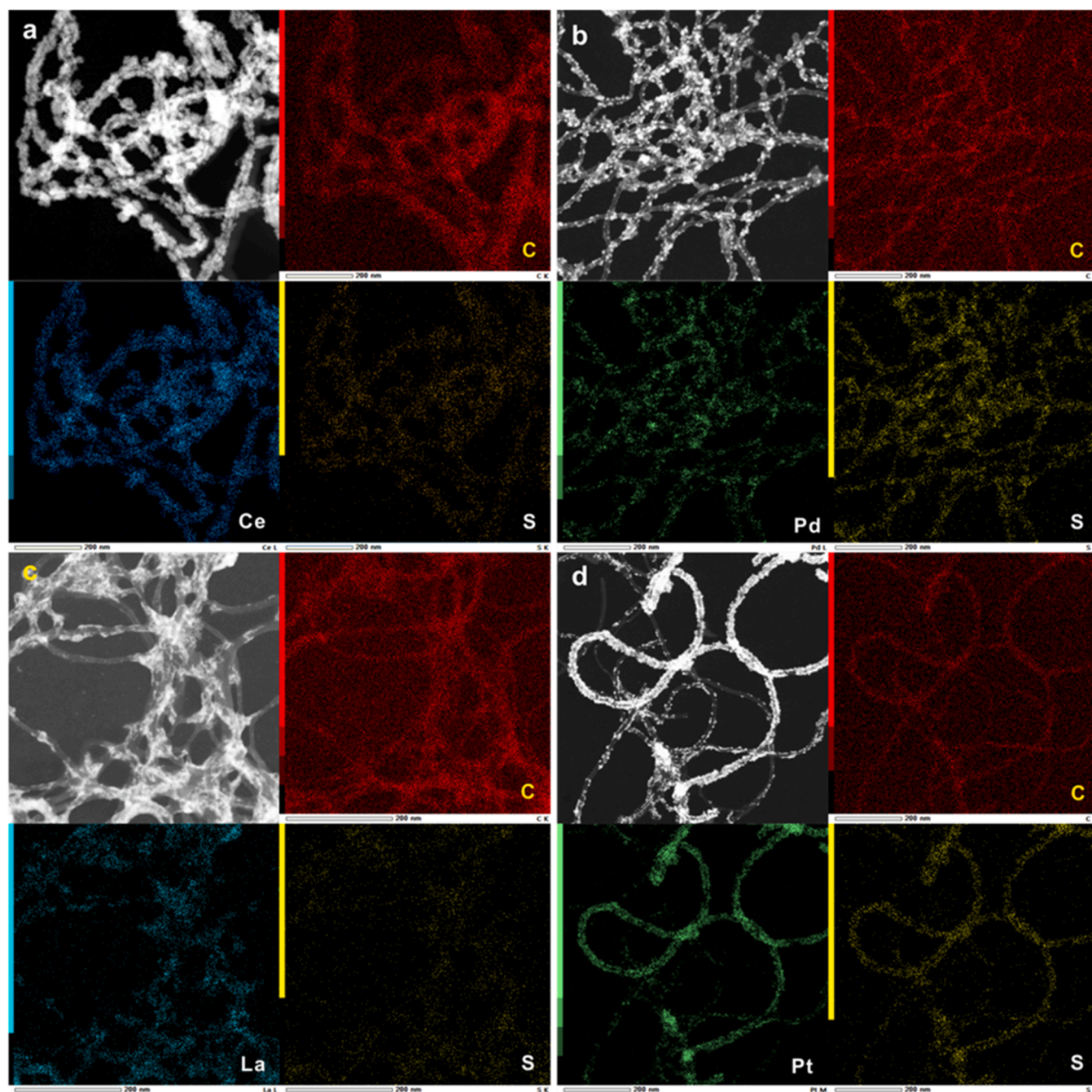


Fig. 7. Microscopic characterizations of heterostructured CNT-MSx (M = Ce, Pd, La, Pt, etc.) synthesized by the in-situ construction strategy. HAADF-STEM image and EDX mapping of (a) CNT-CeSx, (b) CNT-PdSx, (c) CNT-LaSx, and (d) CNT-PtSx.

LaSx, and CNT-PtSx NWs, respectively. It was clear that the entire NWs exhibit CNT like 1D characteristics with ultrathin nanoparticles covered, which are like the heterostructured CNT-RuSx materials. The unique structures and compositions of those as-prepared NWs are also visualized by EDX-mapping analysis. It can be clearly observed that S and M elements are distributed on the surface of C, which also proves that Ce, Pd, La and Pt are successfully captured by S on the surface of CNT. All the results show that in-situ construction strategy has general applicability for the preparation of C-based supported catalysts.

4. Conclusion

In this work, we successfully constructed CNT-RuSx heterostructured electrocatalysts by an in-situ construction strategy, and the synthesis

process is simple and the overall cost is less than traditional Pt-based catalysts. In the process of material preparation, carbon nanotubes as a carrier and a donor of S element directly capture Ru and form amorphous RuSx on its surface to form heterostructured CNT-RuSx materials. Meanwhile, in the catalytic process, element C directly promotes the electrochemical hydrogen evolution of RuSx through the C-S-Ru interface. Due to the existence of abundant C-S-Ru interface, the obtained CNT-RuSx possesses remarkable catalytic hydrogen evolution activity. In 1 M KOH, to output a current density of 10 mA/cm², the required overpotential on the CNT-RuSx is only 17 mV, which is better than that of commercial Pt/C (45 mV). It should be pointed out that excellent catalytic stability is also achieved on CNT-RuSx, when an overpotential of 200 mV is applied the output current density can still be maintained at 320 mA/cm² for 40 h. DFT calculations show that C-S-Ru

heterostructures can effectively dissociate water and promote H-H coupling. This work unambiguously elucidates the catalytic behavior of the heterostructured interface in electrochemical hydrogen evolution, as well as providing a feasible technical guidance for the development of next-generation commercial carbon-supported electrocatalysts.

CRedit authorship contribution statement

Changgen Cheng: Investigation, Data curation, Writing – original draft; **Weidong Ao:** Investigation, Data curation, Validation; **Huijun Ren:** Investigation, Data curation, Validation; **Zhengyuan Shen:** Investigation, Data curation; **Zhishuai Fan:** Investigation; **Tingting Xu:** Investigation; **Wei Liu:** Investigation, Writing – original draft; **Qi Zhang:** Investigation, Resources, Writing – original draft; **Peiqun Yin:** Conceptualization, Resources, Visualization, Writing – original draft, Supervision, Writing – review & editing; **Lei Dai:** Conceptualization, Resources, Visualization, Writing – original draft, Supervision, Writing – review & editing, Project administration, Funding acquisition.

Declaration of Competing Interest

The authors declare that they have no known competing financial interests or personal relationships that could have appeared to influence the work reported in this paper.

Data Availability

Data will be made available on request.

Acknowledgment

We would like to acknowledge the Facility for Analysis, Characterization, Testing, and Simulation, Henan University, China, for use of their electron microscopy (and/or X-ray) facilities. L.D. gratefully acknowledges financial support from the National Natural Science Foundation of China (22202059) and the Start-Up Grants from Henan University. L.D. thanks Dr. Chao Wang in University of science and technology of China, and Prof. Xinsheng Liu in Henan University for their help during the manuscript preparation.

Author Contributions

L.D. and P.Y. proposed the research direction and guided the project. C.C. and W.A. performed the experiments and carried out the electrochemical experiments. Q.Z. performed the theoretical work. W.L. and L.D. performed the XAS characterization and the data fitting and analysis. Z.S., H.R., Z.F. and T.X. carried out parts of the characterizations. C.C., Q.Z., W.L., P.Y. and L.D. analyzed and discussed all experimental results and drafted the manuscript. C.C., W.A., H.R. and Z.S. contributed equally to this work. All the authors contributed to the overall scientific interpretation.

Appendix A. Supporting information

Supplementary data associated with this article can be found in the online version at [doi:10.1016/j.apcatb.2023.122681](https://doi.org/10.1016/j.apcatb.2023.122681).

References

- [1] J. Mahmood, F. Li, S.M. Jung, M.S. Okyay, I. Ahmad, S.J. Kim, N. Park, H.Y. Jeong, J.B. Baek, An efficient and pH-universal ruthenium-based catalyst for the hydrogen evolution reaction, *Nat. Nanotech.* 12 (2017) 441–446.
- [2] Y. Li, J. Zhang, Y. Liu, Q. Qian, Z. Li, Y. Zhu, G. Zhang, Partially exposed RuP₂ surface in hybrid structure endows its bifunctionality for hydrazine oxidation and hydrogen evolution catalysis, *Sci. Adv.* 6 (2020) eabb4197.
- [3] Y. Li, Y. Sun, Y. Qin, W. Zhang, L. Wang, M. Luo, H. Yang, S. Guo, Recent advances on water-splitting electrocatalysis mediated by noble-metal-based nanostructured materials, *Adv. Energy Mater.* 10 (2020), 1903120.
- [4] J. Zheng, W. Sheng, Z. Zhuang, B. Xu, Y. Yan, Universal dependence of hydrogen oxidation and evolution reaction activity of platinum-group metals on pH and hydrogen binding energy, *Sci. Adv.* 2 (2016), e1501602.
- [5] R. Jiang, Y. Da, J. Zhang, H. Wu, B. Fan, J. Li, J. Wang, Y. Deng, X. Han, W. Hu, Non-equilibrium synthesis of stacking faults-abundant Ru nanoparticles towards electrocatalytic water splitting, *Appl. Catal. B: Environ.* 316 (2022), 121682.
- [6] Z. Zhuang, Y. Wang, C.Q. Xu, S. Liu, C. Chen, Q. Peng, Z. Zhuang, H. Xiao, Y. Pan, S. Lu, R. Yu, W.C. Cheong, X. Cao, K. Wu, K. Sun, Y. Wang, D. Wang, J. Li, Y. Li, Three-dimensional open nano-netcage electrocatalysts for efficient pH-universal overall water splitting, *Nat. Commun.* 10 (2019) 4875.
- [7] J. Wang, H. Yang, F. Li, L. Li, J. Wu, S. Liu, T. Cheng, Y. Xu, Q. Shao, X. Huang, Single-site Pt-doped RuO₂ hollow nanospheres with interstitial C for high-performance acidic overall water splitting, *Sci. Adv.* 8 (2022) eab19271.
- [8] J. Wang, H.Y. Tan, T.R. Kuo, S.C. Lin, C.S. Hsu, Y. Zhu, Y.C. Chu, T.L. Chen, J. F. Lee, H.M. Chen, In situ identifying the dynamic structure behind activity of atomically dispersed platinum catalyst toward hydrogen evolution reaction, *Small* 17 (2021), 2005713.
- [9] W. Zang, T. Sun, T. Yang, S. Xi, M. Waqar, Z. Kou, Z. Lyu, Y.P. Feng, J. Wang, S. J. Pennycook, Efficient hydrogen evolution of oxidized Ni-N₃ defective sites for alkaline freshwater and seawater electrolysis, *Adv. Mater.* 33 (2021), 2003846.
- [10] L. Dai, Z.N. Chen, L. Li, P. Yin, Z. Liu, H. Zhang, Ultrathin Ni(OH)₂ heterostructured nanosheets with enhanced electrochemical overall water splitting, *Adv. Mater.* 32 (2020), 1906915.
- [11] J. Yu, Y. Guo, S. She, S. Miao, M. Ni, W. Zhou, M. Liu, Z. Shao, Bigger is surprisingly better: agglomerates of larger RuP nanoparticles outperform benchmark Pt nanocatalysts for the hydrogen evolution reaction, *Adv. Mater.* 30 (2018), 1800047.
- [12] Q. Liang, Q. Li, L. Xie, H. Zeng, S. Zhou, Y. Huang, M. Yan, X. Zhang, T. Liu, J. Zeng, K. Liang, O. Terasaki, D. Zhao, L. Jiang, B. Kong, Superassembly of surface-enriched Ru nanoclusters from trapping-bonding strategy for efficient hydrogen evolution, *ACS Nano* 16 (2022) 7993–8004.
- [13] W. Ao, C. Cheng, H. Ren, Z. Fan, P. Yin, Q. Qin, Z.N. Chen, L. Dai, Heterostructured Ru/Ni(OH)₂ nanomaterials as multifunctional electrocatalysts for selective reforming of ethanol, *ACS Appl. Mater. Interfaces* 14 (2022) 45042–45050.
- [14] P. Li, X. Duan, S. Wang, L. Zheng, Y. Li, H. Duan, Y. Kuang, X. Sun, Amorphous ruthenium-sulfide with isolated catalytic sites for Pt-like electrocatalytic hydrogen production over whole pH range, *Small* 15 (2019), 1904043.
- [15] D.H. Kwon, M.S. Okyay, S.J. Kim, J.P. Jeon, H.J. Noh, N. Park, J. Mahmood, J. B. Baek, Ruthenium anchored on carbon nanotube electrocatalyst for hydrogen production with enhanced Faradaic efficiency, *Nat. Commun.* 11 (2020) 1278.
- [16] J. Yu, Q. He, G. Yang, W. Zhou, Z. Shao, M. Ni, Recent advances and prospective in ruthenium-based materials for electrochemical water splitting, *ACS Catal.* 9 (2019) 9973–10011.
- [17] Y. Sun, Z. Xue, Q. Liu, Y. Jia, Y. Li, K. Liu, Y. Lin, M. Liu, G. Li, C.Y. Su, Modulating electronic structure of metal-organic frameworks by introducing atomically dispersed Ru for efficient hydrogen evolution, *Nat. Commun.* 12 (2021) 1369.
- [18] S. Zhu, X. Qin, F. Xiao, S. Yang, Y. Xu, Z. Tan, J. Li, J. Yan, Q. Chen, M. Chen, M. Shao, The role of ruthenium in improving the kinetics of hydrogen oxidation and evolution reactions of platinum, *Nat. Catal.* 4 (2021) 711–718.
- [19] J. Zhang, X. Mao, S. Wang, L. Liang, M. Cao, L. Wang, G. Li, Y. Xu, X. Huang, Superlattice in a Ru superstructure for enhancing hydrogen evolution, *Angew. Chem. Int. Ed.* 61 (2022), 202116867.
- [20] C.-B. Hong, X. Li, W.-B. Wei, X.-T. Wu, Q.-L. Zhu, Nano-engineering of Ru-based hierarchical porous nanoreactors for highly efficient pH-universal overall water splitting, *Appl. Catal. B: Environ.* 294 (2021), 120230.
- [21] R. Shen, Y. Liu, H. Wen, T. Liu, Z. Peng, X. Wu, X. Ge, S. Mehdi, H. Cao, E. Liang, J. Jiang, B. Li, Engineering VO-Ti ensemble to boost the activity of Ru towards water dissociation for catalytic hydrogen generation, *Appl. Catal. B: Environ.* 306 (2022), 121100.
- [22] X. Wang, A. Vasileff, Y. Jiao, Y. Zheng, S.Z. Qiao, Electronic and structural engineering of carbon-based metal-free electrocatalysts for water splitting, *Adv. Mater.* 31 (2019), 1803625.
- [23] J. Wang, H. Kong, J. Zhang, Y. Hao, Z. Shao, F. Ciucci, Carbon-based electrocatalysts for sustainable energy applications, *Prog. Mater. Sci.* 116 (2021), 100717.
- [24] C.-L. Yang, L.-N. Wang, P. Yin, J. Liu, M.-X. Chen, Q.-Q. Yan, Z.-S. Wang, S.-L. Xu, S.-Q. Chu, C. Cui, Sulfur-anchoring synthesis of platinum intermetallic nanoparticle catalysts for fuel cells, *Science* 374 (2021) 459–464.
- [25] K. Gong, F. Du, Z. Xia, M. Durstock, L. Dai, Nitrogen-doped carbon nanotube arrays with high electrocatalytic activity for oxygen reduction, *Science* 323 (2009) 760–764.
- [26] C. Hu, J. Qu, Y. Xiao, S. Zhao, H. Chen, L. Dai, Carbon nanomaterials for energy and biorelated catalysis: recent advances and looking forward, *ACS Cent. Sci.* 5 (2019) 389–408.
- [27] Y. Bai, H. Yue, J. Wang, B. Shen, S. Sun, S. Wang, H. Wang, X. Li, Z. Xu, R. Zhang, Super-durable ultralong carbon nanotubes, *Science* 369 (2020) 1104–1106.
- [28] G. Valenti, A. Boni, M. Melchionna, M. Cargnello, L. Nasi, G. Berton, R.J. Gorte, M. Marcaccio, S. Rapino, M. Bonchio, P. Fornasiero, M. Prato, F. Paolucci, Co-axial heterostructures integrating palladium/titanium dioxide with carbon nanotubes for efficient electrocatalytic hydrogen evolution, *Nat. Commun.* 7 (2016) 13549.
- [29] Y.M. Chen, X.Y. Yu, Z. Li, U. Paik, X.W. Lou, Hierarchical MoS₂ tubular structures internally wired by carbon nanotubes as a highly stable anode material for lithium-ion batteries, *Sci. Adv.* 2 (2016), e1600021.
- [30] Y. Chen, Z. Lai, X. Zhang, Z. Fan, Q. He, C. Tan, H. Zhang, Phase engineering of nanomaterials, *Nat. Rev. Chem.* 4 (2020) 243–256.

- [31] X. Zhang, Z. Luo, P. Yu, Y. Cai, Y. Du, D. Wu, S. Gao, C. Tan, Z. Li, M. Ren, T. Osipowicz, S. Chen, Z. Jiang, J. Li, Y. Huang, J. Yang, Y. Chen, C.Y. Ang, Y. Zhao, P. Wang, L. Song, X. Wu, Z. Liu, A. Borgna, H. Zhang, Lithiation-induced amorphization of $\text{Pd}_3\text{P}_2\text{S}_8$ for highly efficient hydrogen evolution, *Nat. Catal.* 1 (2018) 460–468.
- [32] Y. He, L. Liu, C. Zhu, S. Guo, P. Golani, B. Koo, P. Tang, Z. Zhao, M. Xu, C. Zhu, P. Yu, X. Zhou, C. Gao, X. Wang, Z. Shi, L. Zheng, J. Yang, B. Shin, J. Arbiol, H. Duan, Y. Du, M. Heggen, R.E. Dunin-Borkowski, W. Guo, Q.J. Wang, Z. Zhang, Z. Liu, Amorphizing noble metal chalcogenide catalysts at the single-layer limit towards hydrogen production, *Nat. Catal.* 5 (2022) 212–221.
- [33] D.J. Morgan, Resolving ruthenium: XPS studies of common ruthenium materials, *Surf. Inter. Anal.* 47 (2015) 1072–1079.
- [34] P. Yin, G. Wu, X. Wang, S. Liu, F. Zhou, L. Dai, X. Wang, B. Yang, Z.-Q. Yu, NiCo-LDH nanosheets strongly coupled with GO-CNTs as a hybrid electrocatalyst for oxygen evolution reaction, *Nano Res.* 14 (2021) 4783–4788.
- [35] H. Jiang, Y. Lin, B. Chen, Y. Zhang, H. Liu, X. Duan, D. Chen, L. Song, Ternary interfacial superstructure enabling extraordinary hydrogen evolution electrocatalysis, *Mater. Today* 21 (2018) 602–610.
- [36] S.C. Ray, H.M. Tsai, J.W. Chiou, B. Bose, J.C. Jan, K. Kumar, W.F. Pong, D. Dasgupta, M.H. Tsai, X-ray absorption spectroscopy (XAS) study of dip deposited a-C:H(OH) thin films, *J. Phys. Cond. Matter* 16 (2004) 5713–5719.
- [37] S. Zhang, F. Ling, L. Wang, R. Xu, M. Ma, X. Cheng, R. Bai, Y. Shao, H. Huang, D. Li, Y. Jiang, X. Rui, J. Bai, Y. Yao, Y. Yu, An open-ended $\text{Ni}_3\text{S}_2\text{-Co}_9\text{S}_8$ heterostructures nanocage anode with enhanced reaction kinetics for superior potassium-ion batteries, *Adv. Mater.* 34 (2022), 2201420.
- [38] L. Cao, Q. Luo, J. Chen, L. Wang, Y. Lin, H. Wang, X. Liu, X. Shen, W. Zhang, W. Liu, Z. Qi, Z. Jiang, J. Yang, T. Yao, Dynamic oxygen adsorption on single-atomic Ruthenium catalyst with high performance for acidic oxygen evolution reaction, *Nat. Commun.* 10 (2019) 4849.
- [39] Y. Xiong, J. Dong, Z.-Q. Huang, P. Xin, W. Chen, Y. Wang, Z. Li, Z. Jin, W. Xing, Z. Zhuang, J. Ye, X. Wei, R. Cao, L. Gu, S. Sun, L. Zhuang, X. Chen, H. Yang, C. Chen, Q. Peng, C.-R. Chang, D. Wang, Y. Li, Single-atom Rh/N-doped carbon electrocatalyst for formic acid oxidation, *Nat. Nanotech.* 15 (2020) 390–397.
- [40] S. Gao, Y. Lin, X. Jiao, Y. Sun, Q. Luo, W. Zhang, D. Li, J. Yang, Y. Xie, Partially oxidized atomic cobalt layers for carbon dioxide electroreduction to liquid fuel, *Nature* 529 (2016) 68–71.
- [41] L. Dai, Q. Qin, P. Wang, X. Zhao, C. Hu, P. Liu, R. Qin, M. Chen, D. Ou, C. Xu, Ultrastable atomic copper nanosheets for selective electrochemical reduction of carbon dioxide, *Sci. Adv.* 3 (2017), e1701069.
- [42] G. Zhao, K. Rui, S.X. Dou, W. Sun, Heterostructures for electrochemical hydrogen evolution reaction: a review, *Adv. Funct. Mater.* 28 (2018), 1803291.
- [43] T.D. Thanh, N.D. Chuong, H. Van Hien, T. Kshetri, N.H. Kim, J.H. Lee, Recent advances in two-dimensional transition metal dichalcogenides-graphene heterostructured materials for electrochemical applications, *Prog. Mater. Sci.* 96 (2018) 51–85.
- [44] D. Chen, R. Yu, R. Lu, Z. Pu, P. Wang, J. Zhu, P. Ji, D. Wu, J. Wu, Y. Zhao, Z. Kou, J. Yu, S. Mu, Tunable Ru-Ru₂P heterostructures with charge redistribution for efficient pH-universal hydrogen evolution, *InfoMat* 4 (2022), e12287.
- [45] J. Wang, Y. Gao, H. Kong, J. Kim, S. Choi, F. Ciucci, Y. Hao, S. Yang, Z. Shao, J. Lim, Non-precious-metal catalysts for alkaline water electrolysis: operando characterizations, theoretical calculations, and recent advances, *Chem. Soc. Rev.* 49 (2020) 9154–9196.
- [46] B. Zhang, J. Liu, J. Wang, Y. Ruan, X. Ji, K. Xu, C. Chen, H. Wan, L. Miao, J. Jiang, Interface engineering: the $\text{Ni}(\text{OH})_2/\text{MoS}_2$ heterostructure for highly efficient alkaline hydrogen evolution, *Nano Energy* 37 (2017) 74–80.
- [47] I. Ledezma-Yanez, W.D.Z. Wallace, P. Sebastián-Pascual, V. Climent, J.M. Feliu, M. T.M. Koper, Interfacial water reorganization as a pH-dependent descriptor of the hydrogen evolution rate on platinum electrodes, *Nat. Energy* 2 (2017) 17031.
- [48] Y. Xue, L. Hui, H. Yu, Y. Liu, Y. Fang, B. Huang, Y. Zhao, Z. Li, Y. Li, Rationally engineered active sites for efficient and durable hydrogen generation, *Nat. Commun.* 10 (2019) 2281.
- [49] C. Wei, S. Sun, D. Mandler, X. Wang, S.Z. Qiao, Z.J. Xu, Approaches for measuring the surface areas of metal oxide electrocatalysts for determining their intrinsic electrocatalytic activity, *Chem. Soc. Rev.* 48 (2019) 2518–2534.
- [50] T. Wu, E. Song, S. Zhang, M. Luo, C. Zhao, W. Zhao, J. Liu, F. Huang, Engineering metallic heterostructure based on Ni_3N and 2M-MoS_2 for alkaline water electrolysis with industry-compatible current density and stability, *Adv. Mater.* 34 (2022), 2108505.